

AD-A143 239

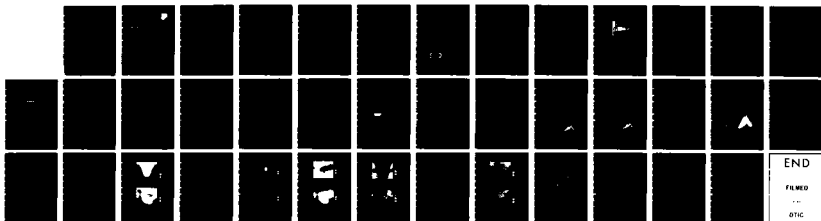
HF PREDICTION USING ADIABATIC INVARIANT THEORY(U) ROME  
AIR DEVELOPMENT CENTER GRIFFISS AFB NY E J TICHOVOLSKY  
MAR 84 RADC-TR-84-59

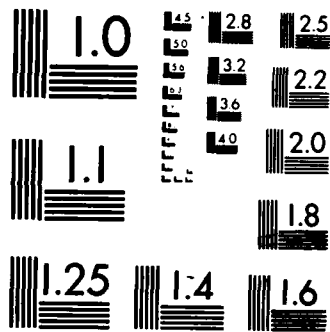
1/1

UNCLASSIFIED

F/G 20/14

NL





MICROCOPY RESOLUTION TEST CHART  
NATIONAL BUREAU OF STANDARDS-1963-A

12

AD-A143 239

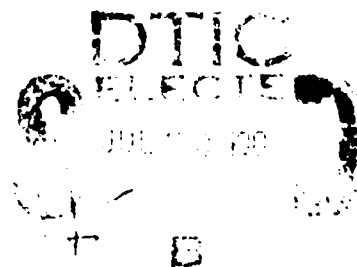
**RADC-TR-84-59**  
**In-House Report**  
**March 1984**



# ***HF PREDICTION USING ADIABATIC INVARIANT THEORY***

**Elihu J. Tichovolsky**

*APPROVED FOR PUBLIC RELEASE; DISTRIBUTION UNLIMITED*



**ROME AIR DEVELOPMENT CENTER**  
**Air Force Systems Command**  
**Griffiss Air Force Base, NY 13441**

DTIC FILE COPY

84 07 15 000

This report has been reviewed by the RADC Public Affairs Office (PA) and is releasable to the National Technical Information Service (NTIS). At NTIS it will be releasable to the general public, including foreign nations.

RADC-TR-84-59 has been reviewed and is approved for publication.

APPROVED:



JOHN E. RASMUSSEN  
Chief, Propagation Branch  
Electromagnetic Sciences Division

APPROVED:



ALLAN C. SCHELL  
Chief, Electromagnetic Sciences Division

FOR THE COMMANDER:



JOHN A. RITZ  
Acting Chief, Plans Office

If your address has changed or if you wish to be removed from the RADC mailing list, or if the addressee is no longer employed by your organization, please notify RADC (EEPI) Hanscom AFB MA 01731. This will assist us in maintaining a current mailing list.

Do not return copies of this report unless contractual obligations or notices on a specific document requires that it be returned.

Unclassified

SECURITY CLASSIFICATION OF THIS PAGE

REPORT DOCUMENTATION PAGE				
1a. REPORT SECURITY CLASSIFICATION Unclassified		1b. RESTRICTIVE MARKINGS		
2a. SECURITY CLASSIFICATION AUTHORITY		3. DISTRIBUTION AVAILABILITY STATEMENT Approved for public release, distribution unlimited.		
2b. DECLASSIFICATION/DOWNGRADING SCHEDULE		4. PERFORMING ORGANIZATION REPORT NUMBER RADC-TR-84-59		
4. PERFORMING ORGANIZATION REPORT NUMBER RADC-TR-84-59		5. MONITORING ORGANIZATION REPORT NUMBER(S)		
6a. NAME OF PERFORMING ORGANIZATION Rome Air Development Center	6b. OFFICE SYMBOL <i>(If applicable)</i> EEPI	7a. NAME OF MONITORING ORGANIZATION		
6c. ADDRESS (City, State and ZIP Code) Hanscom AFB Massachusetts 01731		7b. ADDRESS (City, State and ZIP Code)		
8a. NAME OF FUNDING/SPONSORING ORGANIZATION	8b. OFFICE SYMBOL <i>(If applicable)</i>	9. PROCUREMENT INSTRUMENT IDENTIFICATION NUMBER		
8c. ADDRESS (City, State and ZIP Code)		10. SOURCE OF FUNDING NOS.		
		PROGRAM ELEMENT NO. 61102F	PROJECT NO. 4600	TASK NO. 16
				WORK UNIT NO. 03
11. TITLE (Include Security Classification) HF Prediction Using Adiabatic Invariant Theory				
12. PERSONAL AUTHOR(S) Elihu J. Tichovolsky				
13a. TYPE OF REPORT In-House	13b. TIME COVERED FROM _____ TO _____	14. DATE OF REPORT (Yr., Mo., Day) 1984 March	15. PAGE COUNT 38	
16. SUPPLEMENTARY NOTATION RADC Project Engineer: Elihu J. Tichovolsky, RADC/EEPI.				
17. COSATI CODES			18. SUBJECT TERMS (Continue on reverse if necessary and identify by block number)	
FIELD	GROUP	SUB. GR.	Adiabatic invariant, Potential well, HF propagation, Ducting, Ionogram, Chordal mode, Synoptic maps, Round-the-world, Ground-hop, Trapped mode	
19. ABSTRACT (Continue on reverse if necessary and identify by block number)				
<p>Gurevich and Tsedilina's adiabatic invariant theory for the potential well model of ionospheric HF radiowave propagation is reviewed and applied to a specific round-the-world (RTW) propagation path. Propagation modes (ducting, ground-hop and chordal) are qualitatively deduced from charts of the adiabatic invariants <math>I_F</math>, <math>I_{FE}</math>, <math>I_{(FE+E)}</math> and <math>I_D</math> vs path length. Quantitative results are presented in the form of a simulated RTW ionogram between an elevated source and receiver. In support of RADC's orbiting receiver experiment, the robustness of global HF propagation is displayed in the form of synoptic maps of <math>I_E</math>, <math>I_F</math>, <math>I_{(FE)}</math> and <math>I_D</math>, using the IONCAP median model ionosphere. These maps show the abundance of various propagation modes on a world-wide basis.</p>				
20. DISTRIBUTION/AVAILABILITY OF ABSTRACT UNCLASSIFIED/UNLIMITED <input type="checkbox"/> SAME AS RPT. <input checked="" type="checkbox"/> DTIC USERS <input type="checkbox"/>		21. ABSTRACT SECURITY CLASSIFICATION Unclassified		
22a. NAME OF RESPONSIBLE INDIVIDUAL Elihu J. Tichovolsky		22b. TELEPHONE NUMBER <i>(Include Area Code)</i>	22c. OFFICE SYMBOL	

DD FORM 1473, 83 APR

EDITION OF 1 JAN 73 IS OBSOLETE.

Unclassified

SECURITY CLASSIFICATION OF THIS PAGE

## Contents

1. INTRODUCTION	7
2. GROUND-BASED EXPERIMENTS	8
3. RADC's ORBITING RECEIVER EXPERIMENT	10
4. ADIABATIC INVARIANT THEORY	11
4.1 Propagation Channel Types	12
4.1.1 Ground-Hop Channel	12
4.1.2 Earth-Detached Channels	13
4.2 Snell's Law in the Potential Well	14
4.3 Number of Bound Solutions Inside the Potential Well	14
4.4 Number of Bound Solutions in Sub-Regions of the Potential Well	15
4.4.1 Adiabatic Invariant $I_F$	16
4.4.2 Adiabatic Invariant $I_1$	17
4.4.3 Adiabatic Invariant $I_E$	17
4.4.4 Adiabatic Invariant $I_{FE}$	17
4.4.5 Adiabatic Invariant $I_{FE+E}$	18
4.5 Number of Bound Solutions in Each Propagation Channel	18
4.6 Number of Bound Solutions in Sub-Regions of the Potential Well at Lower Frequencies	19
4.6.1 Propagation Channels at 8 MHz	20
4.6.2 Commonality of the Adiabatic Invariants	20
5. CHANNEL TRACKING	21
6. SIMULATED IONOGRAMS	26
7. ADIABATIC INVARIANT SYNOPTIC MAPS	28
7.1 Synoptic $I_E$ Maps	30
7.2 Synoptic $I_F$ Maps	30
7.3 Synoptic $I_1$ Maps	30
7.4 Synoptic $I_{FE}$ Maps	34
8. CONCLUSION	34
REFERENCES	37

## Illustrations

1.	Schematic Representations of Three Idealized RTW Propagation Modes	5
2.	RTW Echo of FM/CW Signal Radiated Northward From Ava, New York and Received at Verona, New York About 137.5 msec Later	9
3.	Use of Heater-Induced, Field-aligned Plasma Irregularities to Deflect Transmitted Signals Into an Ionospheric Duct	10
4.	Plasma Frequency Profile Over the Point (19.5° S, 6.8° E) From IONCAP With Sunspot Number 50 in June at 12 UT, and the Corresponding Potential Function at $f = 20$ MHz	12
5.	Potential Well at $f = 20$ MHz for the Plasma Frequency Profile in Figure 4 With F-Layer Ground-hop Modes in Channel I, E-Layer Chordal Modes in Channel II, FE-trapped Modes in Channel III, and F-Layer Chordal Modes in Channel IV	13
6.	Computed Relative Adiabatic Invariant vs Energy Level for the Potential Well in Figure 5	16
7.	Potential Well at $f = 8$ MHz for the Plasma Frequency Profile in Figure 4 With F-Layer Ground-hop Modes in Channel I, E-Layer Chordal Modes in Channel II, FE-trapped Modes in Channel III, and E-Layer Ground-hop Modes in Channel V	19
8.	Variation in Solar Zenith Angle, Critical Frequencies and Maximum Electron Density Heights (from IONCAP with Sunspot Number 50 in June at 12 UT) Along a Great Circle Path Heading Due East from (42° N, 120° E) and Passing Through (19.5° S, 6.8° E) at 240 Degrees Angular Range	22
9.	Adiabatic Invariants $I_F$ , $I_1$ , $I_{FE}$ and $I_{FE+E}$ vs Angular Range at $f = 20$ MHz Along the Great Circle Path in Figure 8	22
10.	The Adiabatic Invariants Chart in Figure 9 With Raypaths $AA_1A_2A_3A$ , $BB_1B_2$ , $CC_1C_2$ , $DD_1D_2D_3D_4D_5D_6$ and $LL_1L_2$ Straddling the Longer Great Circle Segment Between the Vertical Dashed Lines at $\theta = 90$ and 240 Degrees	23
11.	Adiabatic Invariants $I_F$ , $I_1$ , $I_{FE}$ and $I_{FE+E}$ vs Angular Range at $f = 8$ MHz Along the Great Circle Path in Figure 8, With RTW Raypaths $AA_1A$ , $BB_1B_2B_3B$ , $CC_1C_2C_3C$ Shown as Horizontal Dashed Lines	25
12.	Simulated, Absorptionless, Swept-frequency RTW Ionogram from an Elevated Source Which is Radiating Due East from (42° N, 120° E)	27
13.	Synoptic Map of Critical Frequency $f_oE$ from IONCAP With Sunspot Number 50 in June at 12 UT	29
14.	Synoptic Map of Critical Frequency $f_oF2$ from IONCAP With Sunspot Number 50 in June at 12 UT	29
15.	Synoptic Map of Adiabatic Invariant $I_E$ at $f = 8$ MHz for the IONCAP Model Ionosphere With Sunspot Number 50 in June at 12 UT	31
16.	Synoptic Map of Adiabatic Invariant $I_E$ at $f = 20$ MHz for the IONCAP Model Ionosphere With Sunspot Number 50 in June at 12 UT	31
17.	Synoptic Map of Adiabatic Invariant $I_F$ at $f = 8$ MHz for the IONCAP Model Ionosphere With Sunspot Number 50 in June at 12 UT	32

### Illustrations

18.	Synoptic Map of Adiabatic Invariant $I_p$ at $f = 20$ MHz for the IONCAP Model Ionosphere With Sunspot Number 50 in June at 12 UT	32
19.	Synoptic Map of Adiabatic Invariant $I_1$ at $f = 8$ MHz for the IONCAP Model Ionosphere With Sunspot Number 50 in June at 12 UT	33
20.	Synoptic Map of Adiabatic Invariant $I_1$ at $f = 20$ MHz for the IONCAP Model Ionosphere With Sunspot Number 50 in June at 12 UT	33
21.	Synoptic Map of Adiabatic Invariant $I_{PE}$ at $f = 8$ MHz for the IONCAP Model Ionosphere With Sunspot Number 50 in June at 12 UT	35
22.	Synoptic Map of Adiabatic Invariant $I_{PE}$ at $f = 20$ MHz for the IONCAP Model Ionosphere With Sunspot Number 50 in June at 12 UT	35
23.	Great Circle Paths Emanating in Various Azimuthal Directions from the Point ( $42^\circ$ N, $120^\circ$ E)	36

### Tables

1.	Propagation Channel Algebra at 20 MHz for the Ionosphere of Figure 4	18
2.	Propagation Channel Algebra at 8 MHz for the Ionosphere of Figure 4	20

**DTIC**  
**ELECTE**  
**S** JUL 20 1984 **D**  
**B**

Accession For	
NTIS GRA&I	<input checked="" type="checkbox"/>
DTIC TAB	<input type="checkbox"/>
Unannounced	<input type="checkbox"/>
Justification	
By _____	
Distribution/	
Availability Codes	
Dist	Avail and/or Special
A-1	



## HF Prediction Using Adiabatic Invariant Theory

### I. INTRODUCTION

The Propagation Branch of the Electromagnetic Sciences Division of RADC is planning to conduct an experiment which will explore the use of low-loss, elevated, ionospheric ducting channels in order to achieve super-long range propagation at HF (6-30 MHz). If successfully exploited, these propagation channels will extend the distances reached in surveillance and communications from one or two hop to round-the-world (RTW).

The purpose of the experiment is to collect swept frequency ionograms which will provide information concerning the modes of the super-long range propagation channels. These modes will be combinations of the three idealized modes shown in Figure 1. The first mode is the classical ground-hop mode in which rays bounce back and forth in the channel between the earth and the ionosphere. The second mode is the chordal mode in which rays are refracted by the ionosphere at angles close enough to the horizontal such that they travel along chords connecting points inside the ionospheric shell and never touch the earth. The third mode is the trapped mode in which rays bounce back and forth in one of the sparsely ionized channels between the relatively denser E, F1 and F2 layers. The chordal and trapped modes are called "earth-detached" modes because their rays never touch the earth. Nevertheless, they can be received (or launched) from the ground

---

(Received for publication 20 March 1984)

in the vicinity of appropriately tilted ionospheric layers that refract them into (or out of) the ground-hop mode.

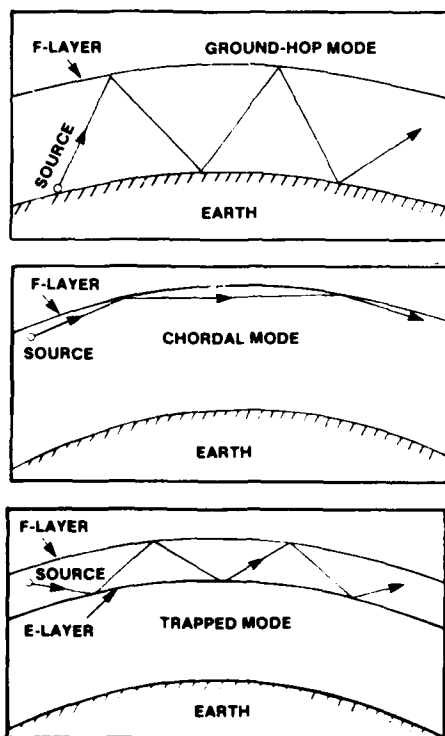


Figure 1. Schematic Representation of Three Idealized RTW Propagation Modes

## 2. GROUND-BASED EXPERIMENTS

Ground-based long range and RTW propagation experiments have provided evidence that ducting takes place.<sup>1, 2</sup> Figure 2 shows a RTW ionogram recorded at 2356 LT during one experiment which involved two neighboring ground stations at Ava and Verona, New York ( $\sim 45^\circ$  N Lat.) that were only 65 km apart.<sup>2</sup> The 137.5 msec delay time of the leading edge indicates that the signal traveled along the longer portion of the connecting North-South great circle. In this successful pass over the auroral zone, the nighttime auroral trough provided a natural

1. Bubenik, D. M., Fraser-Smith, A. C., Sweeney, L. E., Jr., and Villard, O. G., Jr. (1971) Observations of fine structure in high-frequency radio signals propagated around the world, *J. Geophys. Res.* 76(4):1088-1092.
2. Elkins, T. J., Toman, K., and Sales, G. S. (1980) Theoretical and Experimental Studies of HF Ducted Propagation, RADC-TR-80-360, AD A098944.

ionospheric tilt that guided the signal up and over the aurora in which it otherwise would have suffered great absorption. Although ground-hop modes were certainly present, nevertheless the auroral portions of the path must have been traversed via earth-detached modes.

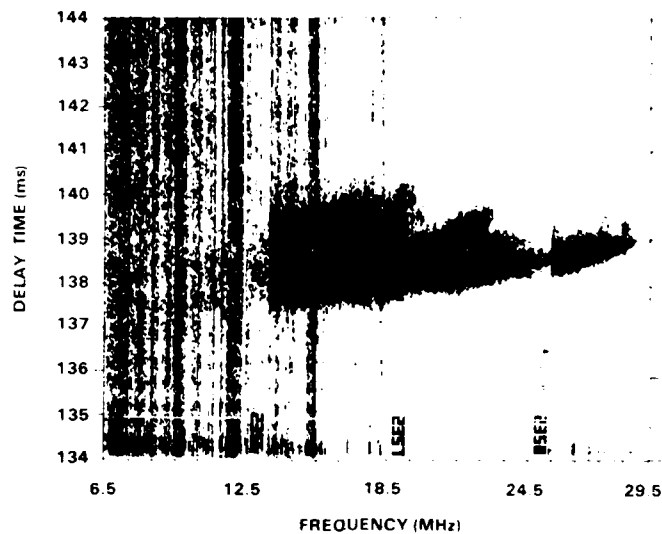


Figure 2. RTW Echo of FM/CW Signal Radiated Northward From Ava, New York and Received at Verona, New York About 137.5 msec Later

Some features of this ionogram are worth noting. The entire visible trace lies within the 2.5 msec time interval between 137.5 and 140 msec delay. The broad vertical lines which run from top to bottom below 13.5 MHz are man-made interference and noise. Beyond 13.5 MHz, where the interference decreases, the gain was manually changed and RTW signals were received out to 25.5 MHz. At the latter frequency the gain was again manually changed and signals were seen to 29 MHz. The splitting of the trace into discrete bands, which end at about 20, 23 and 29 MHz, is typical of RTW ionograms. Tsedilina<sup>3</sup> has theoretically attributed these bands, whose delay times increase with frequency, to ground-hop and chordal modes. On the other hand, she has associated other band structures which exhibit decreased delay times with increasing frequency with trapped modes.<sup>1</sup> However, her conclusions are based upon qualitative, rather than quantitative, matching to the band

3. Tsedilina, Ye. Ye. (1980) Discrete structure of round-the-world signals, Geomagnetism and Aeronomy, 20(1):99-101.

structures. The availability of an elevated, orbiting receiver in the RADC experiment would remove the duct ejection losses which affect ground-based measurements and might result in more detailed ionograms.

### 3. RADC'S ORBITING RECEIVER EXPERIMENT

RADC's experiment calls for signals emitted from a ground-based source to enter one of several possible RTW propagation channels either via a naturally tilted, ionospheric refraction gradient (for example, the solar terminator) or via a nearby, artificially produced, ionospheric scattering region. If necessary, the latter may be created by means of the "heater" shown in Figure 3. The receiver will orbit the earth every 90 min with perigee altitude within the ducting region. Nine long-range ionograms in one 15-min interval per orbit at perigee will be collected and telemetered to earth over a 1-yr period.

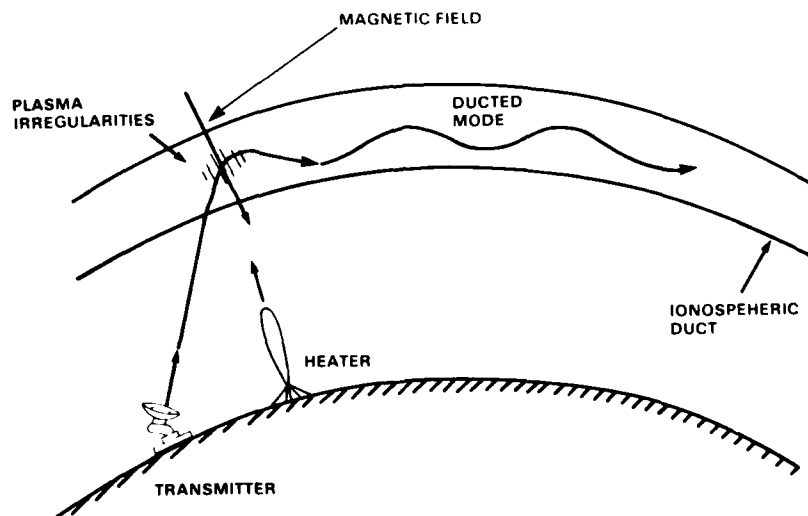


Figure 3. Use of Heater-Induced, Field-aligned Plasma Irregularities to Deflect Transmitted Signals Into an Ionospheric Duct

The success of the experiment depends on advance knowledge of the locations of the most robust ducting channels. Although several transmitter sites will be available during the experiment, the receiver will be able to listen to only one of them at a time. Turn-around time for ionogram telemetry and processing will be about three days. By this time the receiver will have moved through many orbits.

Successful scheduling of the transmitters will require quick and reliable, computational pre-assessment of the relative robustness of the ducting channels to the receiver. Since conventional raytracing would be too slow, we have turned to a technique recently developed for this kind of problem, by researchers in the Soviet Union.

#### 4. ADIABATIC INVARIANT THEORY

The adiabatic invariant technique was pioneered by Gurevich,<sup>4</sup> Tsedilina,<sup>5,5</sup> Fishchuk<sup>6</sup> and others over the past 10 years. It is an outgrowth of earlier work by Wovk.<sup>7</sup> The theory begins with the magnetic vector potential  $\vec{A}(r, \theta, \phi) = \psi(r) Y_{\ell m}(\theta, \phi) \hat{j}$  which is inserted into Maxwell's equations. Here,  $r$  is the radial distance from earth center,  $\theta$  is the polar angle which measures distance along a great-circle path,  $\phi$  is the off-path azimuthal angle,  $\psi$  represents the radial part of  $\vec{A}$ ,  $Y_{\ell m}$  represents the angular part of  $\vec{A}$ , and  $\hat{j}$  is an arbitrary unit vector. After separation of variable and linearization, the spatial dependence of  $\psi(z = r - r_0)$  in a spherically symmetric ionosphere is governed by the one-dimensional Schrodinger equation for a free-particle in a potential well:<sup>8</sup>

$$\frac{d^2 \psi}{dz^2} + k^2 [E - U(z)] \psi = 0, \quad (1)$$

where

$$E = \ell(\ell + 1)/k^2 r_0^2,$$

$$U(z) = -\epsilon(z) - 2z/r_0,$$

$$\epsilon(z) = 1 - f_p^2(z)/f^2,$$

$r_0$  is the earth radius,  $k$  is the free-space wave number,  $f_p(z)$  is the ionospheric plasma frequency and  $f$  is the operating frequency. The negative of the potential well function  $U(z)$  is the sum of the magnetic field-free, collision-free dielectric constant  $\epsilon(z)$  and the "spherical distortion" term  $2z/r_0$ , where  $z$  represents altitude above earth. The "energy level"  $E$  represents the coupling constant to the differential equation for  $Y_{\ell m}$ .

(Due to the large number of references cited above, they will not be listed here. See References, page 37.)

Figure 4 shows how the function  $U(z)$  is constructed. To the left is a plasma frequency profile over the point (19.5°S, 6.8°E) taken from the IONCAP median model ionosphere with sunspot number 50 in June at 1200 UT. The E-layer has been suppressed for clarity. To the right is the corresponding  $U(z)$  profile for an operating frequency of 20 MHz. Notice that the latter profile always begins with  $U = -1$  on the ground and continues along the tilted line  $-2z/r_0$  until significant ionization appears at an altitude of about 80 km. Thereafter, this linear behavior is modified by the E and F2-layer ionizations. If this profile is rotated 90 degrees, as in Figure 5, the outlines of a potential well is immediately apparent.

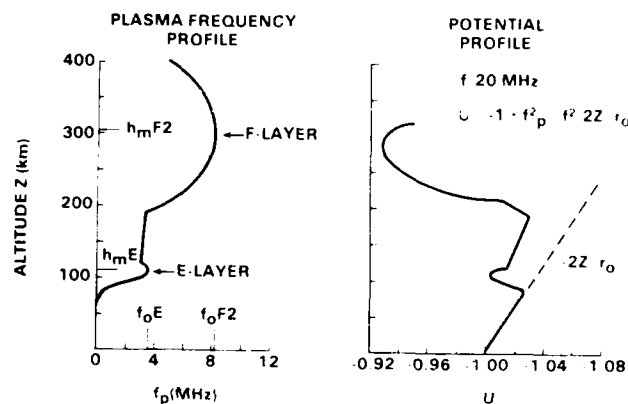


Figure 4. Plasma Frequency Profile Over the Point (19.5°S, 6.8°E) from IONCAP With Sunspot Number 50 in June at 12 UT, and the Corresponding Potential Function at  $f = 20$  MHz

#### 4.1 Propagation Channel Types

##### 4.1.1 GROUND-HOP CHANNEL

In Figure 5, the vertical portion of the left-hand wall, which extends from  $U = -1$  to  $U = \infty$ , corresponds to the perfectly reflective ground. The right-hand wall stops at  $z_F$ , where  $U$  attains the maximum value  $E_F$ . Therefore, the wave-reversing portion of the bottomside of the F-layer lies below the horizontal line  $U = E_F$ , because this line represents the maximum level for bound solutions. Levels lying above  $U = E_F$  correspond to unbound solutions which penetrate through the

9. Lloyd, J.L., Haydon, G.W., Lucas, D.L., and Teters, L.R. Estimating the Performance of Telecommunication Systems Using the Ionospheric Transmission Channel, Vol. 1, Techniques for Analyzing Ionospheric Effects Upon HF Systems (to be published by NTIA/ITS).

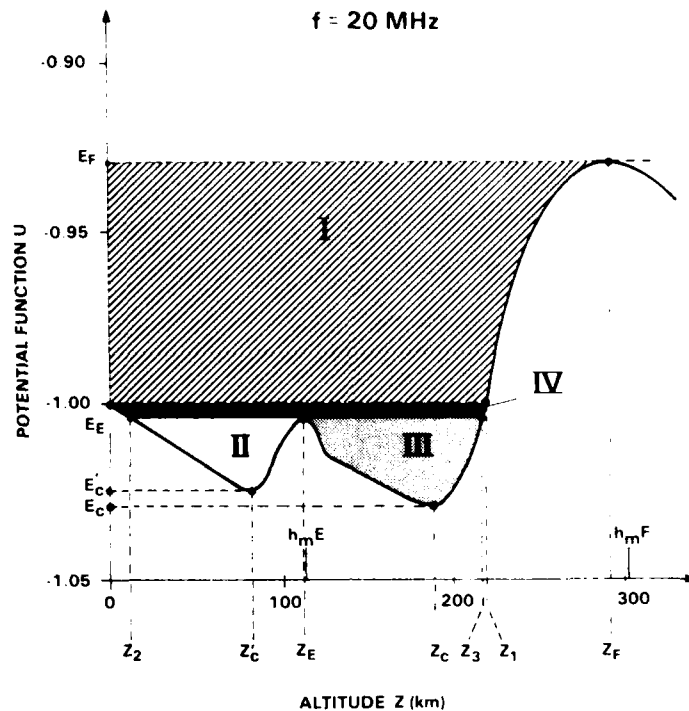


Figure 5. Potential Well at  $f = 20$  MHz for the Plasma Frequency Profile in Figure 4 With F-Layer Ground-hop Modes in Channel I, E-Layer Chordal Modes in Channel II, FE-trapped Modes in Channel III, and F-Layer Chordal Modes in Channel IV. The E- and F-Layer maximum electron density heights are  $h_m^E$  and  $h_m^F$ , respectively

ionosphere, while levels lying between  $U$  and  $E_E$  and  $U = -1$  correspond to bound solutions which bounce back and forth between the ground and the ionosphere. The latter levels belong to the F-layer ground-hop channel which we shall call Channel I. Below the line  $U = -1$ , the left-hand wall is detached from the ground. Consequently, we shall refer to the corresponding levels as earth-detached levels.

#### 4.1.2 EARTH-DETACHED CHANNELS

The earth-detached levels are divided among three different channels due to the presence of the secondary maximum  $U = E_E$  at  $z_E$ . From  $U = -1$  down to  $U = E_E$ , F-layer ionization produces the right-hand wall while the upper portion of the "pseudo wall" term  $-2z/r_0$ , which contains no ionization, accounts for the left-hand wall. Therefore, these levels correspond to the F-layer chordal mode channel which we will call Channel IV. Beneath Channel IV lie two more channels both of

which extend downwards from the line  $U = E_{11}$ . Channel II, on the left, is the E-layer chordal mode channel which lies between the lower portion of the  $-2z/r_0$  pseudo wall and the wave-reversing portion of the bottomside of the E-layer. To the right, between the topside of the E-layer and the lower portion of the bottomside of the F-layer, lies Channel III, which is a trapped mode channel. If an F1 layer were present, additional channels would exist, but these were suppressed in order to simplify this discussion.

#### 4.2 Snell's Law in the Potential Well

Snell's Law in a spherical, stratified ionosphere is  $\mu r \sin i = \text{const}$ , where  $\mu = \sqrt{\epsilon}$  is the index of refraction and  $i$  is the vertical incidence angle. Since  $\epsilon \approx 1$  and  $\mu r = \sqrt{\epsilon} r^2 = r_0 \sqrt{\epsilon(1+z/r_0)^2} \approx r_0 \sqrt{\epsilon(1+2z/r_0)} \approx r_0 \sqrt{\epsilon + 2z/r_0} = r_0 \sqrt{-U}$ , then  $\sqrt{-U} \cos \alpha \approx \text{const}$ , where  $\alpha$  is the elevation angle complementary to  $i$  and is measured away from the horizontal plane passing through the altitude  $z$  corresponding to  $E = U(z)$ . Suppose we set  $\text{const} = \sqrt{-E_c} \cos \alpha_c$  at the reference altitude  $z_c$ , where  $E_c = U(z_c)$  represents a minimum in  $U$ . Then on total reflection,  $\alpha = 0$ , and therefore  $\alpha_c \approx \cos^{-1} \sqrt{E/E_c}$  gives the ray's elevation angle as it passes through  $z_c$ .

For rays which do not hit the ground,  $\alpha = 0$  occurs at two different altitudes which define the upper reflection point  $z_u$ , where  $U(z_u) = E$ , and the lower reflection point  $z_l$ , where  $U(z_l) = E$  also. On the other hand, for ground-hop rays,  $\alpha = 0$  is still true at the upper reflection point, but no longer on the ground. Let us move the reference altitude down to the ground, where  $U = -1$ , and set  $\text{const} = \sqrt{1} \cos \beta$ , where  $\beta$  is the ground launch or arrival angle. Then,  $\alpha = 0$  yields  $\beta = \cos^{-1} \sqrt{-E}$ .

We can use  $\alpha_c$ ,  $z_c$  and  $\beta$  to provide reasonable initial guesses for ray-trace calculations. More significantly, having established a correspondence between energy levels in our potential well and rays propagating in the pertinent ionospheric channels, we can turn to the problem of measuring the robustness of these channels - that is, counting the number of rays (or equivalently, the number of energy levels) which each channel can accommodate.

#### 4.3 Number of Bound Solutions Inside the Potential Well

The adiabatic invariant theory enables us to count the total number of energy levels inside the potential well by applying the WKB solution to Eq. (1). Outside the well, beyond the turning points,  $E < U(z)$  and this solution consists of damped exponentials,

$$\begin{aligned} \psi(z) &= 1/2 C [iK(z)]^{-1/2} \exp \left[ i \int_{z_u}^z K(z) dz \right], \quad z \gg z_u, \text{ and} \\ \psi(z) &= 1/2 C' [iK(z)]^{-1/2} \exp \left[ i \int_z^{z_l} K(z) dz \right], \quad z \ll z_l, \end{aligned} \quad (2)$$

where  $K(z) = k\sqrt{I - U(z)}$ ,  $C$  and  $C'$  are arbitrary constants, and  $z_l$  and  $z_u$  are, respectively, the lower and upper turning points defined in Section 4.2. Inside the well, between the turning points, there are two possible kinds of bound solutions:

$$\psi(z) = C[K(z)]^{-1/2} \cos \left[ \int_z^{z_u} K(z) dz - \pi/4 \right]$$

and

$$\psi(z) = C'[K(z)]^{-1/2} \cos \left[ \int_{z_l}^z K(z) dz - \pi/4 \right], \quad z_l \leq z \leq z_u. \quad (3)$$

These match the outside solutions only if  $kl_n = (n + 1/2)\pi$ ,

where

$$I_n = \int_{z_l}^{z_u} \sqrt{E_n - U(z)} dz, \quad E_0 \cong E_n \cong E_N \quad (4)$$

and  $n = 0, 1, 2, \dots, N$  is the number of possible nodes in  $\psi_n$ . The number  $n$  also counts the number of eigenvalues corresponding to bound solutions. We see that there are a total of  $N+1$  eigenvalues in the spherically symmetric ionosphere assumed in Eq. (1).

As an aside, we note that action integrals of the form  $\int P_z dz$ , where

$$P_z = \sqrt{2m(E - U)} = \text{phase space momentum and}$$

$$z = \text{phase-space position,}$$

when applied to periodic systems are called "adiabatic invariants". Hence, the use of this name for integrals like  $I_n$ .

#### 4.4 Number of Bound Solutions in Sub-Regions of the Potential Well

In Figure 6 we show  $I$  vs  $E$  for the potential well of Figure 5. We shall drop the index  $n$  and consider  $I$  and  $E$  to be continuous because  $l \approx 10$  to  $10^2$  km, while  $\lambda = 2\pi/k \approx 10$  m, and therefore,  $kl \approx 10^3$  to  $10^4$  levels. For added convenience, we shall ignore the multiplicative constant  $k$  and merely let  $I$  represent a relative number of bound solutions. We see that  $I$  varies continuously from the upper cutoff (point 5, corresponding to  $E_1$ ) down to the lower cutoff (point 3, corresponding to  $E_E$ ).

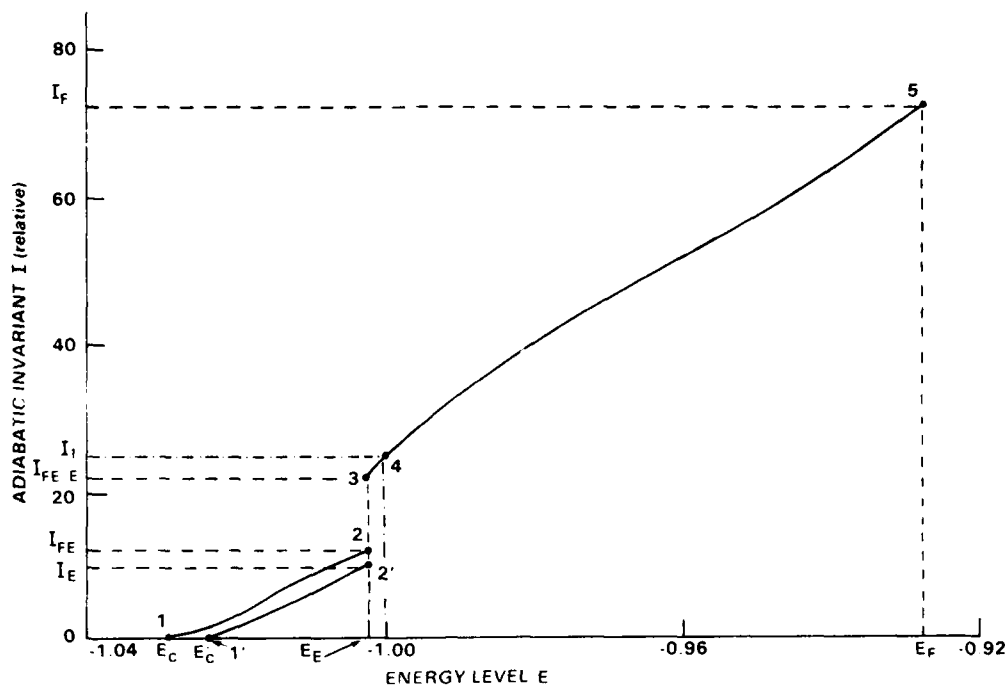


Figure 6. Computed, Relative Adiabatic Invariant vs Energy Level for the Potential Well in Figure 5

From Figure 5 we know that this curve actually spans two channels: between points 5 and 4 it lies in Channel I, and between points 4 and 3 it lies in Channel IV. Immediately below point 3 there is a gap in  $I$  because the potential well splits into two subwells. This splitting makes  $I$  a double-valued function of  $E$ : the curve between points 1 and 2 lies in Channel III, while the curve between points 1' and 2' lies in Channel II. The gap in  $I$  occurs even though there is no corresponding discontinuity in  $E$ . We will discuss the implications of this fact in Section 5. For the moment, let us look at some special values of  $I$  in more detail.

#### 4.4.1 ADIABATIC INVARIANT $I_F$

The number of bound solutions belonging to the entire well is

$$I_F = \int_0^{z_F} \sqrt{E_F - U(z)} dz, \quad (5)$$

Where  $E$  in Eq. (4) was set to the largest, finite, maximum value  $E_F$ , and the integration runs between the infinitely high ground wall at  $z = 0$  and the altitude  $z_F$ , at which  $U = E_F$ , as shown in Figure 5. Recall that for  $E > E_F$ , solutions can escape over the right-hand well wall—that is, they penetrate through the ionosphere and are lost.

#### 4.4.2 ADIABATIC INVARIANT $I_1$

The second adiabatic invariant is

$$I_1 = \int_0^{z_1} \sqrt{-1 - U(z)} dz, \quad (6)$$

where  $U$  was set to the value  $-1$ , and the integration runs between the ground, on which  $U = -1$ , and the ionospheric altitude  $z_1$  at which the multivalued function  $U$  is again equal to  $-1$ . The number  $I_1$  includes bound solutions which are all detached from the earth, since  $U < -1$  for these solutions. It also must include the grazing solution, at  $U = -1$ , that hits the ground horizontally. If this grazing solution does not exist (that is, for a  $U(z)$  profile with  $U < -1$  for all  $z > 0$ ), then  $I_1$  will be defined equal to zero. This does not mean that there are no detached solutions in this case. To the contrary, the only possible bound solutions would indeed be detached modes! However, all of these solutions would already have been included in  $I_1$ , and therefore, we set  $I_1 = 0$  to indicate this. On the other hand, for profiles in which  $U$  varies above and below  $-1$  (such as in Figure 5),  $I_1$  will serve to segregate ground-hop solutions, for which  $U > -1$  from detached mode solutions, for which  $U < -1$ .

#### 4.4.3 ADIABATIC INVARIANT $I_E$

The third adiabatic invariant is

$$I_E = \int_{z_2}^{z_E} \sqrt{E_E - U(z)} dz, \quad (7)$$

where  $E$  was set to the secondary, maximum value  $E_E$ , and the integration runs between the two altitudes  $z_2$  and  $z_E$ , both of which lie beneath the E-layer and are intercepted by the line  $U = E_E$ . Thus,  $I_E$  is proportional to the number of bound solutions which in this particular case are chordal modes beneath the E-layer in Channel II in Figure 5.

#### 4.4.4 ADIABATIC INVARIANT $I_{FE}$

The fourth adiabatic invariant is

$$I_{FE} = \int_{z_E}^{z_3} \sqrt{E_E - U(z)} dz, \quad (8)$$

where  $E_E$  is the same secondary, maximum value used above for  $I_E$ , and the integration runs between the previously mentioned altitude  $z_E$  and the altitude  $z_3$  where the lower portion of the F-layer is intercepted by the continuation of the line  $U = E_E$ . Hence,  $I_{FE}$  is proportional to the number of trapped mode solutions caught between the E and the F-layers in Channel III in Figure 5.

#### 4.4.5 ADIABATIC INVARIANT $I_{FE+E}$

It is of interest to note that the same energy level  $E_E$  was used in defining both  $I_E$  and  $I_{FE}$ . Consequently, the latter two may be summed to form a fifth adiabatic invariant  $I_{FE+E} = I_E + I_{FE}$  which represents the sum of the bound solutions associated with the presence of the E-layer. The quantities  $I_{FE+E}$  and  $I_{FE}$  straddle the gap between points 2 and 3 in Figure 6. This gap shrinks at night when the E-layer thins out and the secondary maximum in  $U$  at  $z_E$  flattens. In general, as the ionosphere becomes depleted of electrons,  $I_F$ ,  $I_E$ ,  $I_{FE}$ , and  $I_{FE+E}$  all decrease continuously. However, as noted in Section 4.3.2,  $I_1$  may abruptly become zero if the ionosphere loses enough electrons to the point where it no longer supports the grazing solution.

#### 4.5 Number of Bound Solutions in Each Propagation Channel

The adiabatic invariants  $I_E$  and  $I_{FE}$  were immediately identified with the number of solutions in Channels II and III of Figure 5. On the other hand, it is possible to count the number of ground-hop solutions in Channel I by subtracting the number of earth-detached solutions  $I_1$  from the total number of solutions  $I_F$ . Likewise, the number of F-layer chordal solutions in Channel IV may be counted by subtracting both the number of E-layer chordal solutions  $I_E$  and the number of trapped solutions  $I_{FE}$  from  $I_1$ . Table 1 below summarizes the "algebra" for all of the channels at 20 MHz for the ionosphere of Figure 4.

Table 1. Propagation Channel Algebra at 20 MHz for the Ionosphere of Figure 4

Channel No.	Channel Type	Relative Number of solutions
I	F-layer ground hop	$I_F - I_1$
II	E-layer chordal	$I_E$
III	E-layer/F-layer trapped	$I_{FE}$
IV	F-layer chordal	$I_1 - I_{FE+E}$

At this point we the important result that we have estimated the number of bound solutions within each channel in this spherically symmetric ionosphere without ever having traced a single ray.

4.6 Number of Bound Solutions in Sub-Regions of the Potential Well at Lower Frequencies

The foregoing analysis was carried out for 20 MHz, a fairly high frequency. At a lower frequency, say 8 MHz, we would expect to find a deeper potential well containing even more bound solutions than at 20 MHz. Also, we would expect to find some ground-hop solutions below the E-layer as well as below the F-layer. This is indeed the case, as shown in Figure 7.

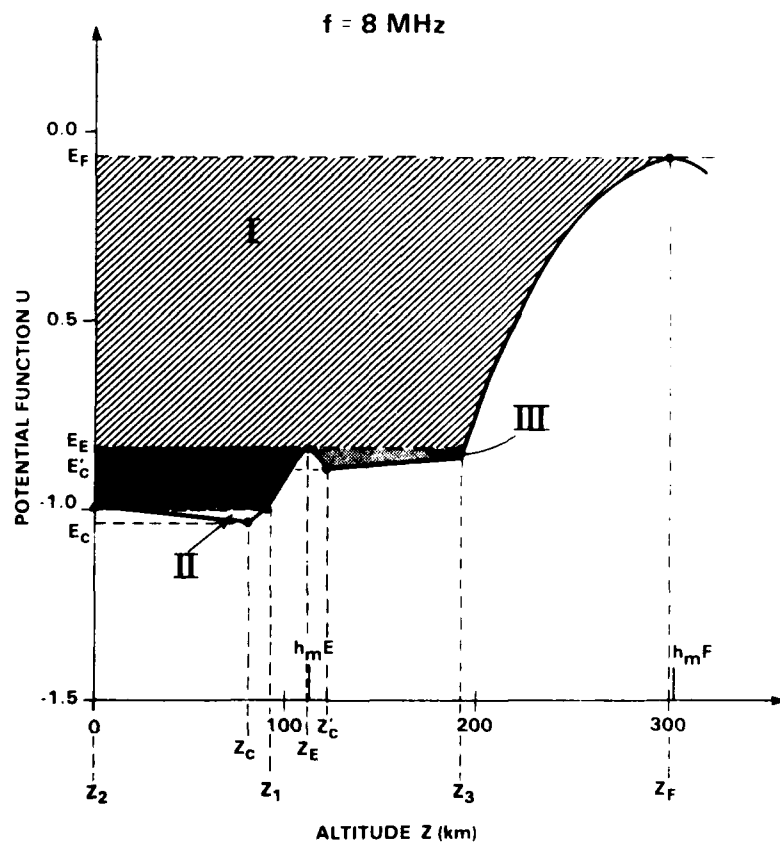


Figure 7. Potential Well at  $f = 8 \text{ MHz}$  for the Plasma Frequency Profile in Figure 4 With F-Layer Ground-hop Modes in Channel I, E-Layer Chordal Modes in Channel II, FE-trapped Modes in Channel III, and E-Layer Ground-hop Modes in Channel V. The E- and F-layer maximum electron density heights are  $h_{mE}$  and  $h_{mF}$ , respectively

#### 4.6.1 PROPAGATION CHANNELS AT 8 MHz

We see from Figure 7 that some of the propagation channels defined in section 4.1 had to be revised. For example, Channel I (F-layer ground-hop solutions), which extended at 20 MHz from  $E_{F_1}$  down to  $U = -1$ , now only goes as far down as  $E_E$ . The maximum energy level limiting Channel II (E-layer chordal solutions) now lies at  $U = -1$ . The definition of Channel III (trapped solutions) remains unchanged, but Channel IV (F-layer chordal solutions) has completely disappeared due to E-layer screening. We also created a new Channel V to describe the new E-layer ground-hop solutions which now fill the region from  $E_{F_1}$  down to  $U = -1$ . At this point, there seems to be no means for comparing the potential wells at the two frequencies in Figures 5 and 7.

#### 4.6.2 COMMONALITY OF THE ADIABATIC INVARIANTS

In spite of the differences in well topology at the two frequencies, the formal definitions given in Section 4.3 for  $I_E$ ,  $I_F$ ,  $I_{FE}$  and  $I_1$  apply to both wells. The only circumstantial changes involve the values of the integration limits and the fixed constants in the kernels. Therefore, we can still use the four adiabatic invariants as basis elements from which to construct a new channel algebra at 8 MHz as given in Table 2.

Table 2. Propagation Channel Algebra at 8 MHz for the Ionosphere of Figure 4

Channel No.	Channel Type	Relative Number of Solutions
I	F-layer ground-hop	$I_F - I_{FE+E}$
II	E-layer chordal	$I_1$
III	E-layer/F-layer trapped	$I_{FE}$
IV	E-layer ground hop	$I_E - I_1$

We could go on to examine even more exotic well topologies and accumulate (or eliminate) additional propagation channels. However, we would find that the four adiabatic invariants  $I_E$ ,  $I_F$ ,  $I_{FE}$  and  $I_1$  form a complete set of elements which we can use in linear combinations to count the solutions belonging to these channels. We shall therefore use these adiabatic invariants to compare different ionospheres over different parts of the globe at the same or at different frequencies.

## 5. CHANNEL TRACKING

The foregoing analysis applied to a spherically symmetric ionosphere. Let us extend this analysis to a set of points along a particular path around the world. Figure 8 shows the variations in solar zenith angle  $\chi$ , layer heights and critical frequencies vs angular range  $\theta$  along the RTW path which heads due east from (42° N, 120° E) at  $\theta = 0$  and passes through the ionosphere of Figure 4 at  $\theta = 240$  degrees. Figure 9 shows the sequential values of the overhead adiabatic invariants  $I_F$ ,  $I_{F+E}$  and  $I_1$  which were computed assuming that the ionosphere was locally spherically symmetric at each point  $\theta$  along the path. The curves were made for  $f = 20$  MHz. We see that this path cannot be entirely traversed at this frequency via ground-hop modes, because we find path segments along which  $I_1$  vanishes. Recall that where  $I_1$  exists, the solutions counted by  $I_F$  are divided into two sets: ground-hop solutions with  $I_1 < I \leq I_F$ , and chordal solutions with  $I < I_1$ . On the other hand, where  $I_1$  vanishes, only chordal solutions are possible.

The lightly hatched regions in Figure 9 show where ground-hopping is permitted. Notice that it is forbidden along the path segment between  $\theta = 90$  degrees and  $\theta = 180$  degrees. Furthermore, at  $\theta = 143$  degrees the only possible propagation mode consists of a very small set of chordal solutions lying in an extremely shallow earth-detached well. This shallow well controls the entire RTW propagation channel for this path at 20 MHz because all ground-hop and many chordal and trapped rays penetrate through it and are lost. As we can see, the adiabatic invariant theory gives us at least a qualitative picture of the survivable propagation modes. The meaning of  $I(\theta)$  can be extended as follows.

The fundamental theorem of the adiabatic invariant approximation states that the bound solution  $\psi_n(z, \theta)$  associated with  $I_n(z, \theta) = \text{const.}$  propagates in a slowly varying ionosphere in accordance with Snell's Law; conversely,  $\psi_n(z, \theta)$  undergoes a transition to another  $\psi_m(z, \theta)$  associated with another  $I_m(\theta) = \text{const.}$  only via a sudden, scattering process which violates Snell's Law. A formal proof of this theorem is not yet available. The ionosphere has to be slowly varying because we will assume that it is locally symmetric about the radius through any particular surface coordinates  $(\theta, \phi)$  for the spatial extent of at least one period of ray oscillation,  $\Theta$ . By "period of oscillation" we mean the distance interval required for a ray to depart and return to the same layer. Examples are the great-circle lengths of either one hop in a ground-hop channel, one complete bounce out and back between the two layers of a trapped mode channel, or one ricochet from and back to the single layer of a chordal mode channel.

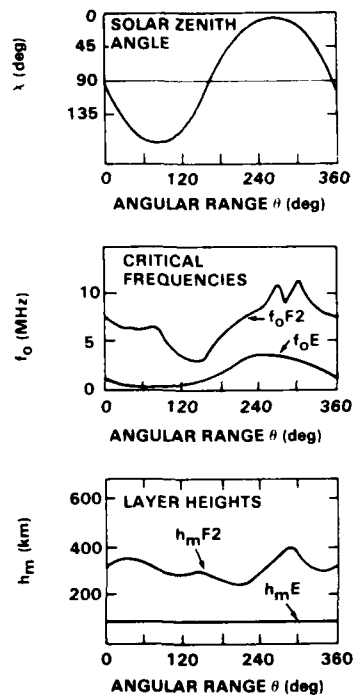


Figure 8. Variation in Solar Zenith Angle, Critical Frequencies and Maximum Electron Density Heights (from IONCAP with Sunspot Number 50 in June at 12 UT) Along a Great Circle Path Heading Due East from (42° N, 120° E) and Passing Through (19.5° S, 6.8° E) at 240 Degrees Angular Range

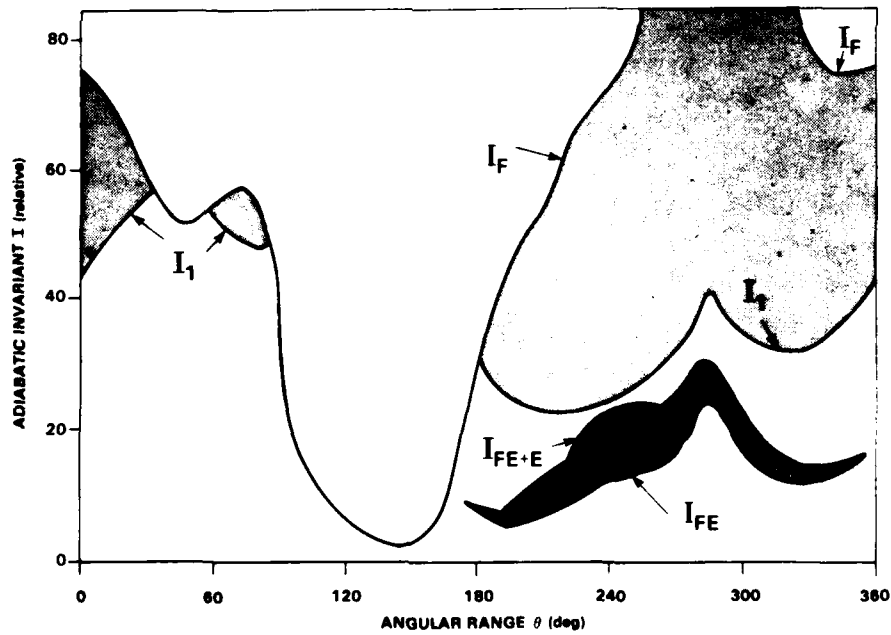


Figure 9. Adiabatic Invariants  $I_F$ ,  $I_1$ ,  $I_{FE}$  and  $I_{FE+E}$  vs Angular Range at  $f = 20$  MHz Along the Great Circle Path in Figure 8

We have already established the relationship between Snells' Law and  $E_n$ , and therefore,  $I_n$ , in Section 4.2 for a symmetric ionosphere. Hence, in the symmetric case, we have a unique ray which traverses the altitude  $z_c$  at the local elevation angle  $\alpha_c$  corresponding to  $I_n$ . We shall assume that this is still approximately true in the nearly symmetric case, and that  $E_n(\theta)$ ,  $\alpha_c(\theta)$ ,  $z_c(\theta)$ ,  $z_u(\theta)$  and  $z_e(\theta)$  readjust in such a way as to leave  $I_n(\theta)$  invariant.

Therefore, the adiabatic invariant approach allows us to "ray-trace"<sup>5</sup> simply by superimposing horizontal lines corresponding to constant values of  $I(\theta)$  upon Figure 9 as shown in Figure 10. By moving either eastward or westward along one of these lines we can immediately determine the propagation modes of the corresponding ray. For example, the segment  $A_3A_1A_2$ , along which  $I(\theta) = 2.5$ , describes a nearly horizontal ray that ricochets in a chordal mode near the bottom of the nighttime F-layer since  $I(\theta) = 2.5$  corresponds to very low-lying levels  $E(\theta)$  and very shallow elevation angles  $\alpha_c(\theta)$ . In daytime along  $A_2A_3$ , this ray becomes trapped between the E- and the F-layers since  $2.5 < I_{FE}(\theta)$ . The foregoing is similarly true for all rays within the band  $I(\theta) \leq 2.5$ .

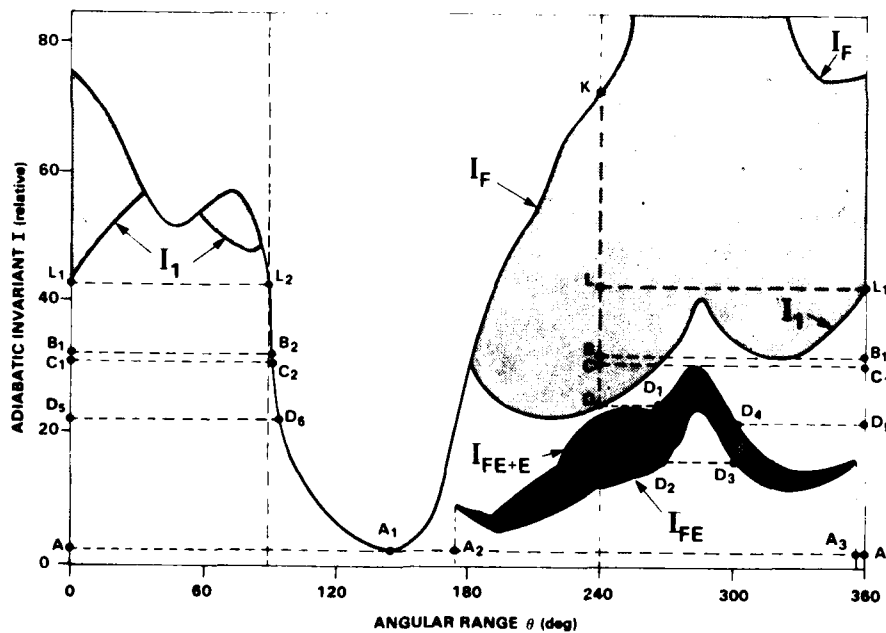


Figure 10. The Adiabatic Invariants Chart in Figure 9 With Raypaths  $AA_1A_2A_3A$ ,  $BB_1B_2$ ,  $CC_1C_2$ ,  $DD_1D_2D_3D_4D_5D_6$  and  $LL_1L_2$  (shown as horizontal dashed lines) Straddling the Longer Great Circle Segment Between the Vertical Dashed Lines at  $\theta = 90$  and  $240$  Degrees

On the other hand, rays with  $l(\theta) > 2.5$  leave the ionosphere somewhere along this RTW path. For example, ray  $B_1B_2$  leaves at  $B_2$ , either by directly penetrating through the F-layer or by first bouncing off the ground and then penetrating somewhat farther along the path. This uncertainty, which could be resolved by actually doing the raytracing, is of no concern as long as we know that this ray is ultimately lost. Indeed, the advantage of the adiabatic invariant theory lies in its ability to deal with the question of existence more directly than the constructive approach of ray-tracing.

To examine a more practical case, suppose we are located on the ground near  $\theta = 240$  degrees and we wish to transmit to an orbiting receiver near  $\theta = 90$  degrees. We first draw two vertical dashed lines, at  $\theta = 240$  degrees and  $\theta = 90$  degrees in Figure 10, and then, begin a process of eliminating rays (in other words, horizontal lines) which emanate from the vertical line at  $\theta = 240$  degrees until we find an unimpeded propagation channel. Since we wish to transmit from the ground, only line segment DCBLK, which lies in the ground-hop channel, is of any use. All horizontal lines pointing westward from DCBLK penetrate through the ionosphere before  $\theta = 180^\circ$ . Therefore, we need to consider only eastward pointing rays. Of the latter, only the rays lying below  $LL_1L_2$  reach  $\theta = 90$  degrees; those above  $LL_1L_2$  penetrate through the F-layer before  $\theta = 90$  degrees. Hence, we are left with segment DCBL. We might also consider the option of eliminating the rays between lines  $BB_1B_2$  and  $LL_1L_2$ , because they involve some ground-hopping between  $BB_1$  and  $LL_1$  that increases the likelihood of D- and E-layer absorption.

The rays between lines  $DD_1$  and  $CC_1$  are controversial because they eventually fall into the gap (darkened region) between  $I_{FE}$  and  $I_{FE+E}$ . In Section 4.4 it was pointed out that  $I$  underwent a sudden discontinuity within this gap, although the level E did not. There are two possible points of view regarding this situation. The liberal view<sup>10,5</sup> maintains that there is a possibility that in traversing point  $D_1$  the ray continues to obey Snell's Law while gradually converting from chordal to trapped mode. This process is schematically represented by the vertical line  $D_1D_2$ . It then proceeds in trapped mode from  $D_2$  to  $D_3$ , where it encounters another gap in  $I$  and reverts to chordal mode, in a process represented by  $D_3D_4$ . Finally the ray continues along  $D_4D_5D_6$  in a chordal mode. On the other hand, a conservative view would hold that all of this is unlikely, and that the only indisputably open, low absorption channel lies between lines  $CC_1C_2$  and  $BB_1B_2$ . Perhaps the RADC experiment will shed light on this issue.

10. Lobachevskiy, L.A., Soares, J., Tushentsova, I.A. Fishchuk, D.I., and Tsedilina, Ye. Ye. (1979) Analysis of the conditions of propagation of decametric radio waves on a long path by the adiabatic method on a fixed frequency. I, Geomagnetism and Aeronomy, 19(3):314-319.

A more exhaustive analysis of this communication channel would require us to redraw Figure 10 at frequencies above and below 20 MHz in order to find the optimum frequency which would make this channel most robust—that is, the frequency which yields the widest band of acceptable  $I$  values. Also, we should generate additional adiabatic invariant charts for other times of day, seasons, sunspot numbers, and so on. Because of lack of space, we will consider only one more case at  $f = 8$  MHz.

From Figure 11 we see that at 8 MHz there exists an earth-detached channel, similar to the one at 20 MHz, below line  $AA_1A$ . It also consists partly of F-layer chordal modes and partly of trapped modes. However, at 8 MHz the E-layer is more influential and the trapped modes predominate. Compare the longer  $I_{FE}$  curve in Figure 11 with the shorter curve in Figure 9. In addition to this RTW channel, we find another, which consists purely of ground-hop rays, between lines  $CC_1C_2C_3C$  and  $BB_1B_2B_3B$ . We might consider adopting this channel for communicating, either eastward or westward, between  $\theta = 240$  degrees and  $\theta = 90$  degrees (vertical dashed lines in Figure 11) via ground-hopping. The westward

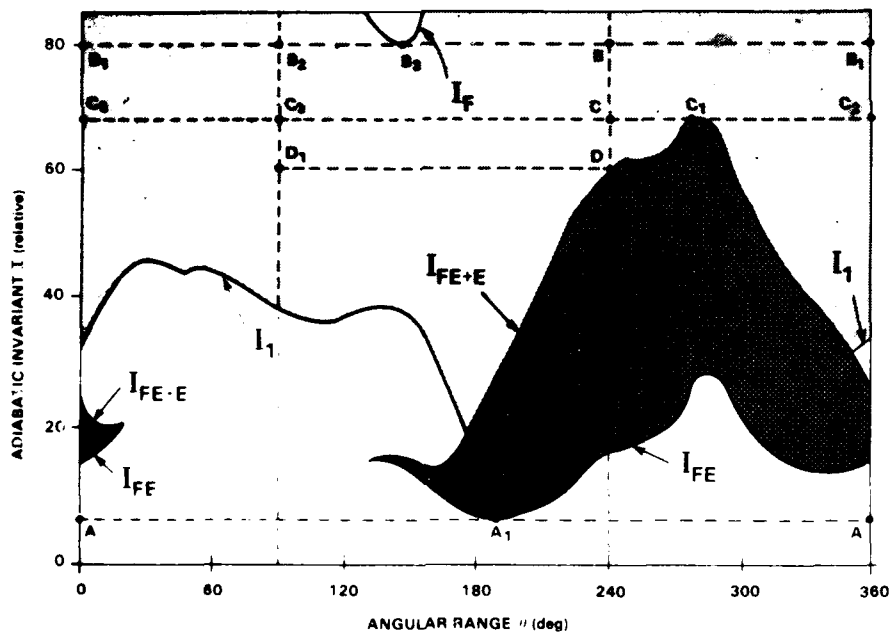


Figure 11. Adiabatic Invariants  $I_F$ ,  $I_1$ ,  $I_{FE}$  and  $I_{FE+E}$  vs Angular Range at  $f = 8$  MHz Along the Great Circle Path in Figure 8, With RTW Raypaths  $AA_1A$ ,  $BB_1B_2B_3B$ ,  $CC_1C_2C_3C$  Shown as Horizontal Dashed Lines. The shorter raypaths  $BB_2$ ,  $CC_3$  and  $DD_1$  straddle the shorter great circle segment between the vertical dashed lines

direction would be preferable because it is shorter and we could include additional rays between DD<sub>1</sub> and CC<sub>3</sub>. However, D- and E-layer absorption would probably preclude any successful ground-hopping. Therefore, we see that, at 8 MHz, ground to elevated receiver communication would be difficult. Again, it is important to realize that we have arrived at these conclusions without having done any actual ray-tracing.

## 6. SIMULATED IONOGRAMS

If we prepare additional charts, similar to Figures 9 and 11, for other frequencies in the HF band and superimpose upon them horizontal lines of constant  $I$ , then we can construct a simulated ionogram between two points, using a procedure described by Fishchuk and Tsedilina.<sup>6</sup> For each frequency we determine the minimum  $I_{\min}$  and the maximum  $I_{\max}$  for the path in question. We consider only  $I$  values between the two lines  $I(\theta) = I_{\min}$  and  $I(\theta) = I_{\max}$ . For each intermediate line  $I(\theta)$ , we compute the corresponding curves  $E(\theta)$ ,  $z_l(\theta)$  and  $z_u(\theta)$  by working backwards from Eq. (4). This task is easy to do if we can interpolate within a precomputed table of these quantities. We then insert the appropriate values into Borisov's<sup>11</sup> formulas for group delay:

$$t_g = \frac{r_0}{c} \int_0^{\theta_f} \left( 1 + \frac{2\bar{z}}{r_0} \right) \frac{d\theta}{\sqrt{-E}}, \quad (9)$$

$$\bar{z} = \frac{2}{r_0 \omega} \int_{z_l}^{z_u} \frac{z dz}{\sqrt{E - U}}, \quad (10)$$

and

$$\omega = \frac{2}{r_0} \int_{z_l}^{z_u} \frac{dz}{\sqrt{E - U}}, \quad (11)$$

where  $t_g$  is the group delay in msec,  $c$  is the speed of light in km/msec,  $r_0$  is earth radius in km,  $\theta_f$  is the path end point in radians,  $\bar{z}$  is the ray "mean altitude" in km and  $\omega$  is the period of ray oscillation in radians.

11. Borisov, N. D., Fishchuk, D. I., and Tsedilina, Ye. Ye. (1978) Frequency dependence of the group lag time of round-the-world signals, Radiophysics and Quantum Electronics, 21(3):255-260.

At this point we have indiscriminately counted all of the rays borne by the ionosphere between  $\theta = 0$  and  $\theta = \theta_c$ . We need to eliminate those rays which do not emanate from the source and those that do not arrive at the receiver. To do this, we keep track of the number of oscillations experienced by each ray via

$$P = \int_0^{\theta_f} d\theta / \theta, \quad (12)$$

and we accept only those rays for which  $P$  is an integer. In this way the simulated ionogram will represent a point-to-point transmission.

The simulated, lossless ionogram in Figure 12 is a preliminary result and will be refined in future work. We see signatures of rays which undergo from 14 to 33 hops RTW lying within the trailing and leading edge (dashed curves) for ground-hop propagation. These results are similar to those first obtained by Fishchuk and Tsedelina.<sup>6</sup> In addition to these ground-hop details, we have also computed the trapped and chordal mode structures. These appear as two bands of simulated signatures: one, immediately below 140 msec and at frequencies less than 12.5 MHz, includes rays which undergo from 14 to 20 periods of oscillation RTW; while the other, immediately above 137 msec, includes from 20 to 26 periods. These bands merge into one band which lies between 138 and 139 msec from 12.5 to 33 MHz. These results do not match those of Tsedelina<sup>3</sup> for trapped modes, as far as delay times and structure are concerned.

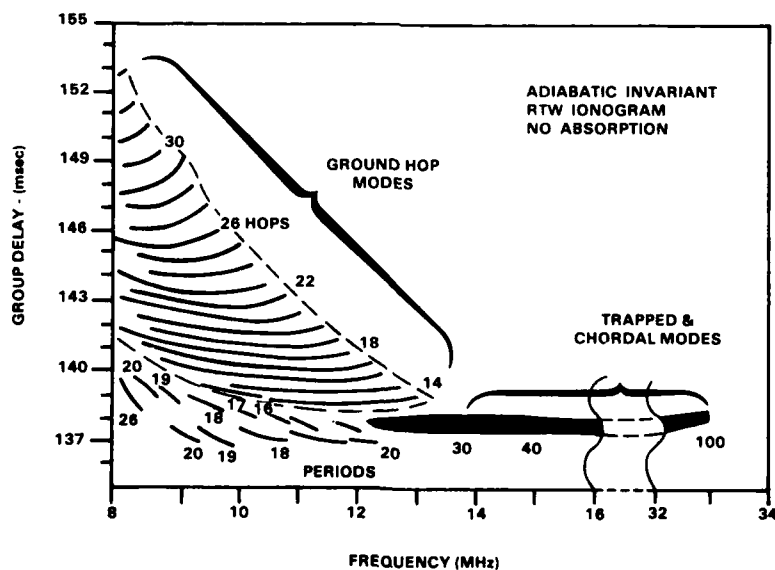


Figure 12. Simulated, Absorptionless, Swept-frequency, RTW Ionogram from an Elevated Source Which is Radiating Due East from (42° N, 120° E)

It is premature to compare Figure 12 with the empirical ionogram in Figure 3. The paths and ionospheric conditions were not the same, and the earth-detached mode structure as shown in Figure 12 needs more work. However, we can find nothing in Figure 12 which resembles the three prominences above 20 MHz in Figure 3. Tsedilina qualitatively attributed these prominences to surviving ground-hop modes but her quantitative results predicted that they should lie below 13 MHz.<sup>3</sup>

## 7. ADIABATIC INVARIANT SYNOPTIC MAPS

Ionograms are suitable for predicting operating frequencies over the path between two given points. For the purpose of assessing propagation robustness between a fixed point and points in a variety of azimuthal directions, a synoptic view is preferable. Here is where the real power of the adiabatic invariant technique was demonstrated by Tushentsova.<sup>12</sup>

Figures 13 and 14 are synoptic maps of  $f_oE$  and  $f_oF2$ , respectively, using the IONCAP model ionosphere for June with sunspot number 50 at 1200 UT, in a format similar to the one used by NBS to show critical frequency contours.<sup>13</sup> For visual impact, bands of adjacent critical frequencies were shaded in tones of gray, instead of labelling each contour line. Also in this format, Figures 15 through 22 show synoptic maps of  $I_E$ ,  $I_F$ ,  $I_1$ , and  $I_{FE}$  at two frequencies—8 and 20 MHz. The gray tones in the latter figures indicate bands of adjacent I values. Some unlabelled contours were drawn inside the broader shaded bands in order to avoid blurring out various topological details. The dot-dash curves in Figures 13 through 22 represent the solar terminator, while the dashed curves denote the RTW path discussed in Section 5. By applying the overlay in Figure 23 to Figures 13 through 22, variations in the ionosphere and in the related propagation modes along great-circle paths in all azimuthal directions that emanate from the starting point at (42° N, 120° E), may be compared.

12. Tushentsova, I. A., Fishchuk, D. I., and Tsedilina, Ye. Ye. (1974) Maps of the global distribution of some parameters of ionospheric wave ducts, Preprint No. 5, IZMIRAN.

13. Zacharisen, D. H. World maps of F2 critical frequencies and maximum usable frequency factors, NBS Tech. Note 2 (Apr 1959) and NBS Tech. Note 2/2 (Oct 1960).

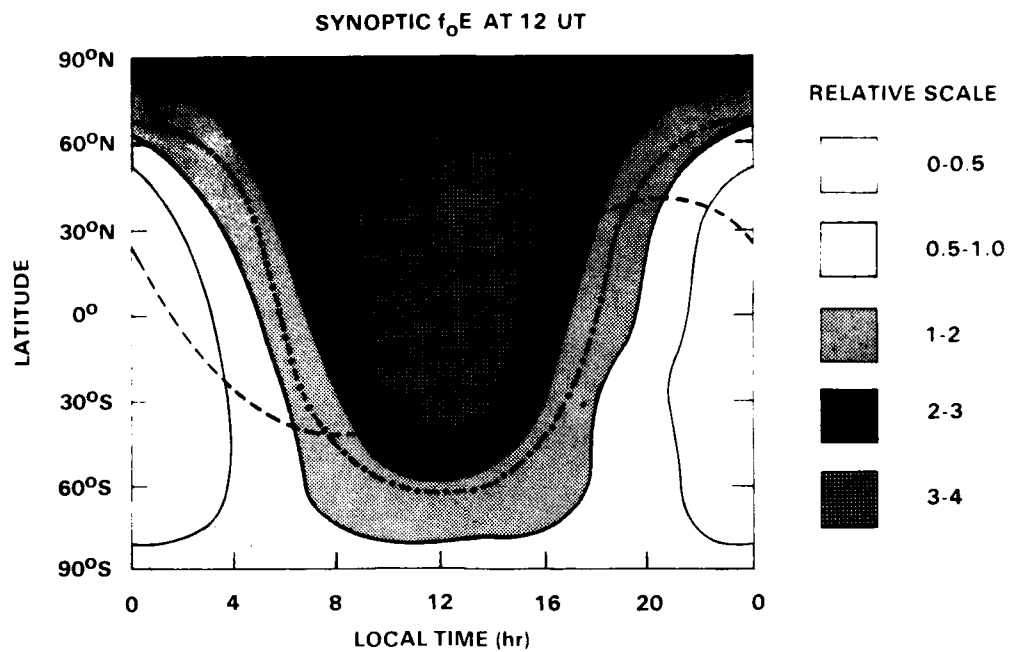


Figure 13. Synoptic Map of Critical Frequency  $f_oE$  from IONCAP With Sunspot Number 50 in June at 12 UT

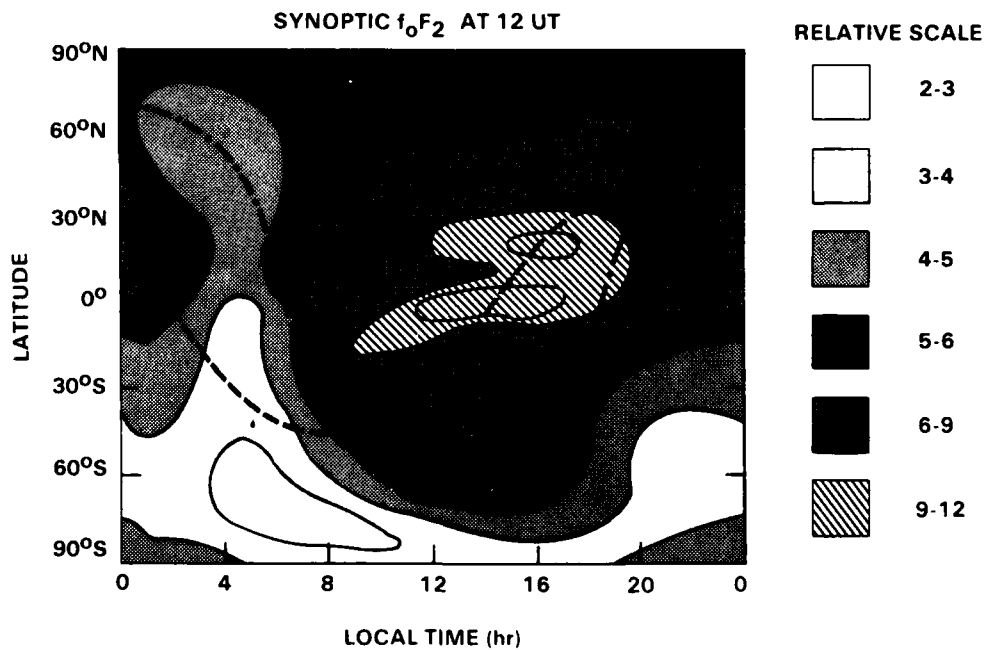


Figure 14. Synoptic Map of Critical Frequency  $f_oF_2$  from IONCAP With Sunspot Number 50 in June at 12 UT

### 7.1 Synoptic $I_E$ Maps

The maps of  $I_E$  (Figure 15 for 8 MHz and Figure 16 and 20 MHz) show the relative robustness of HF propagation via ground-hop and/or chordal modes involving the bottomside of the global E-layer. The contour regions in these  $I_E$  maps conform to those of  $f_{\text{O}E}$  in Figure 13. To further distinguish between ground-hop and chordal modes, it would be necessary to compare these maps with those for  $I_1$  in Figures 19 and 20, as will be done in Section 7.3.

### 7.2 Synoptic $I_F$ Maps

The maps of  $I_F$  (Figure 17 for 8 MHz and Figure 18 for 20 MHz) show the relative robustness of total HF propagation anywhere over the globe, irrespective of the mode type or the ionospheric layer involved. The  $I_F$  contours resemble those for  $f_{\text{O}F2}$  in Figure 14; the most robust regions occur in the vicinity of the Appleton anomalies, where the F2-layer is densest and highest; while the least robust regions occur at the poles and in the nighttime hemisphere. The effects of the auroral zones are not visible because IONCAP lacks a realistic model auroral ionosphere. The robustness of the groundhop and/or chordal modes that exclusively involve the F-layer, (without in anyway involving the E-layer) may be measured by adding the  $I_E$  and  $I_{FE}$  maps together and then subtracting this sum from the corresponding  $I_F$  map at the same frequency.

### 7.3 Synoptic $I_1$ Maps

The maps of  $I_1$  (Figure 19 for 8 MHz and Figure 20 for 20 MHz) show where chordal modes exist either by themselves ( $I_1 = 0$ ) or together with ground-hop modes ( $I_1 > 0$ ). While  $I_1$  may vary continuously within the gray regions ( $I_1 > 0$ ), the transition from gray to white ( $I_1 = 0$ ) occurs abruptly at points where the ionosphere has just become depleted of sufficient electrons to refract the grazing solutions back to earth, as was discussed in Section 4.4.2.

By subtracting  $I_1$  (only in the regions where  $I_1 \neq 0$ ) from  $I_E$  for the corresponding geographical areas, it is possible to obtain a map of the robustness of the E-layer ground-hop modes. It is also possible to obtain a similar map of exclusively F-layer ground-hop modes, by first subtracting both  $I_E$  and  $I_{FE}$  from  $I_F$ , and then, subtracting  $I_1$  (only in the regions where  $I_1 \neq 0$ ) from the resulting map. Of course, ground-hopping is forbidden in the remaining regions where  $I_1 = 0$ .

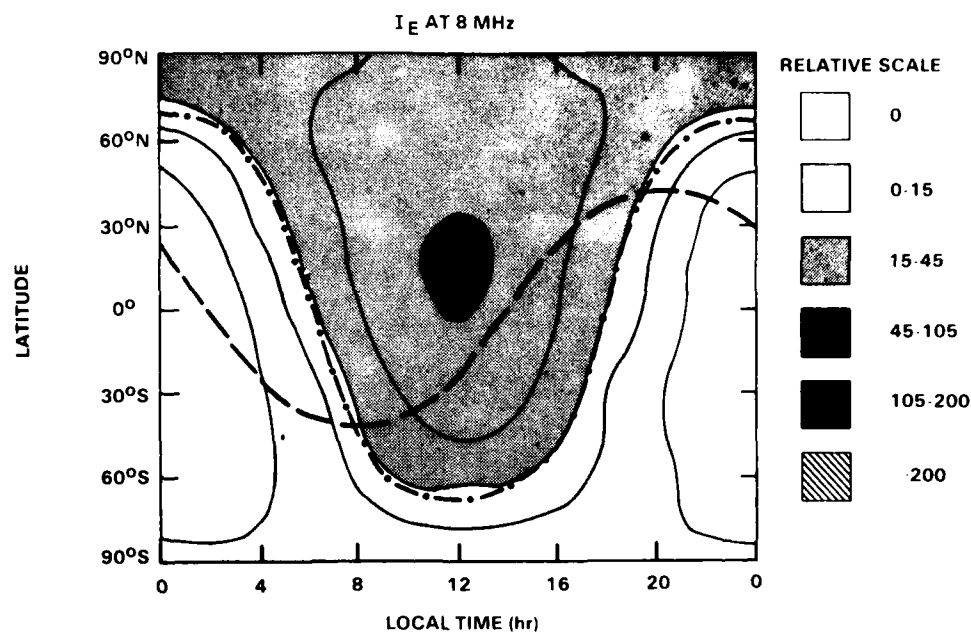


Figure 15. Synoptic Map of Adiabatic Invariant  $I_E$  at  $f=8$  MHz for the IONCAP Model Ionosphere With Sunspot Number  $E_{50}$  in June at 12 UT

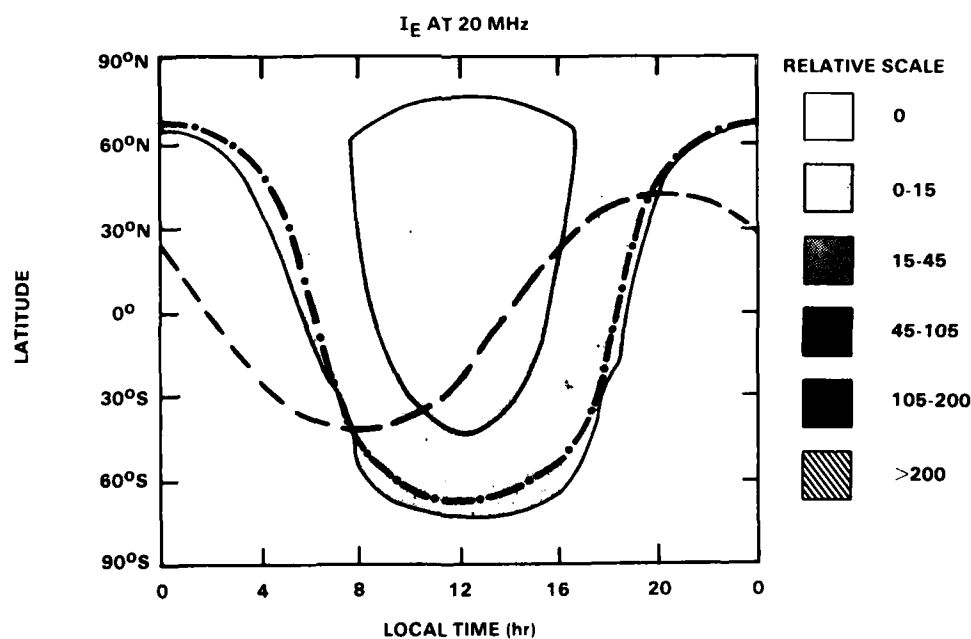


Figure 16. Synoptic Map of Adiabatic Invariant  $I_E$  at  $f=20$  MHz for the IONCAP Model Ionosphere With Sunspot Number  $E_{50}$  in June at 12 UT

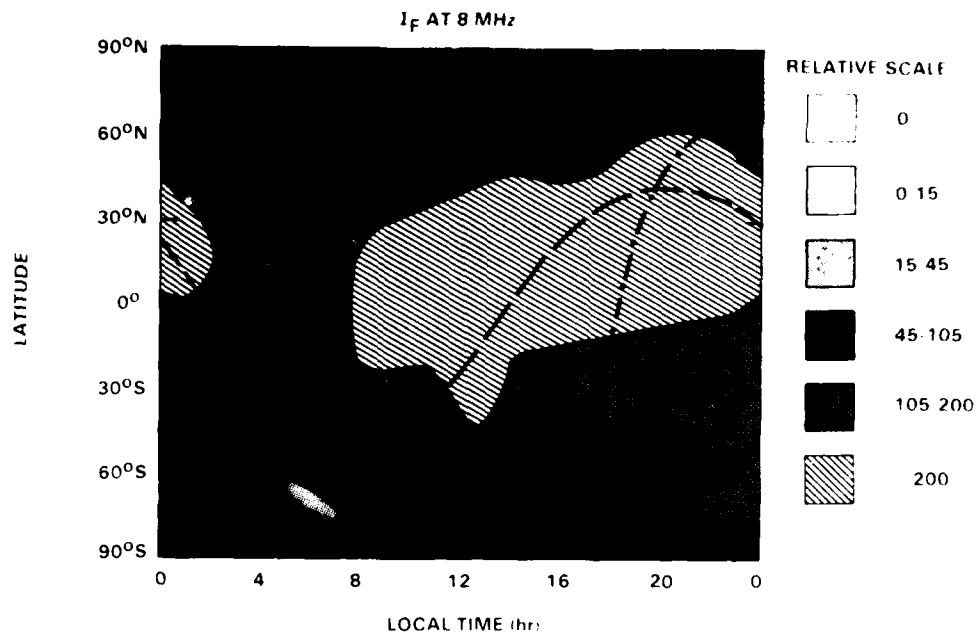


Figure 17. Synoptic Map of Adiabatic Invariant  $I_F$  at  $f=8$  MHz for the IONCAP Model Ionosphere With Sunspot Number 50 in June at 12 UT

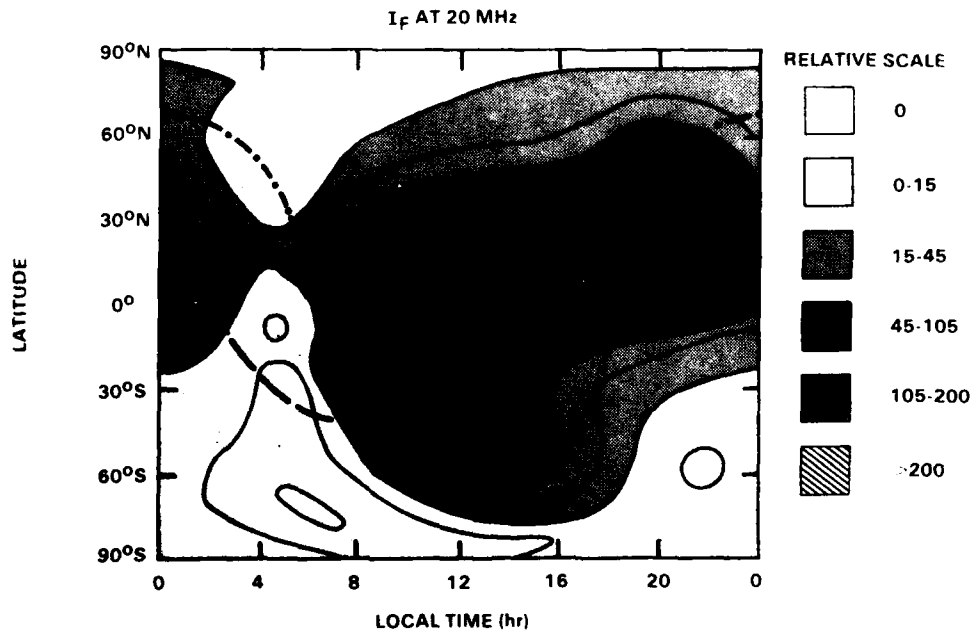


Figure 18. Synoptic Map of Adiabatic Invariant  $I_F$  at  $f=20$  MHz for the IONCAP Model Ionosphere With Sunspot Number 50 in June at 12 UT

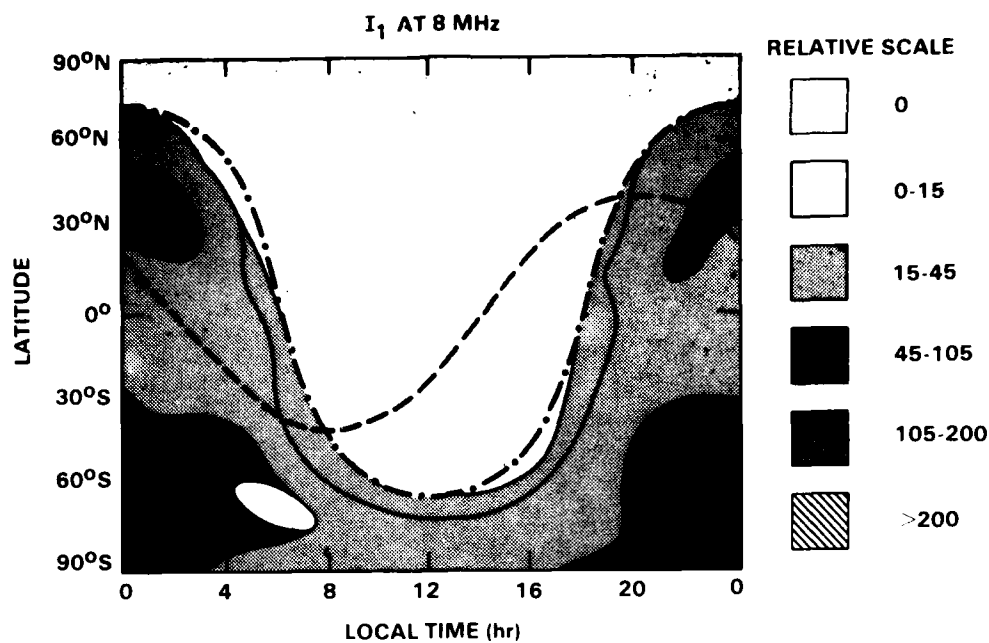


Figure 19. Synoptic Map of Adiabatic Invariant  $I_1$  at  $f=8$  MHz for the IONCAP Model Ionosphere With Sunspot Number 50 in June at 12 UT

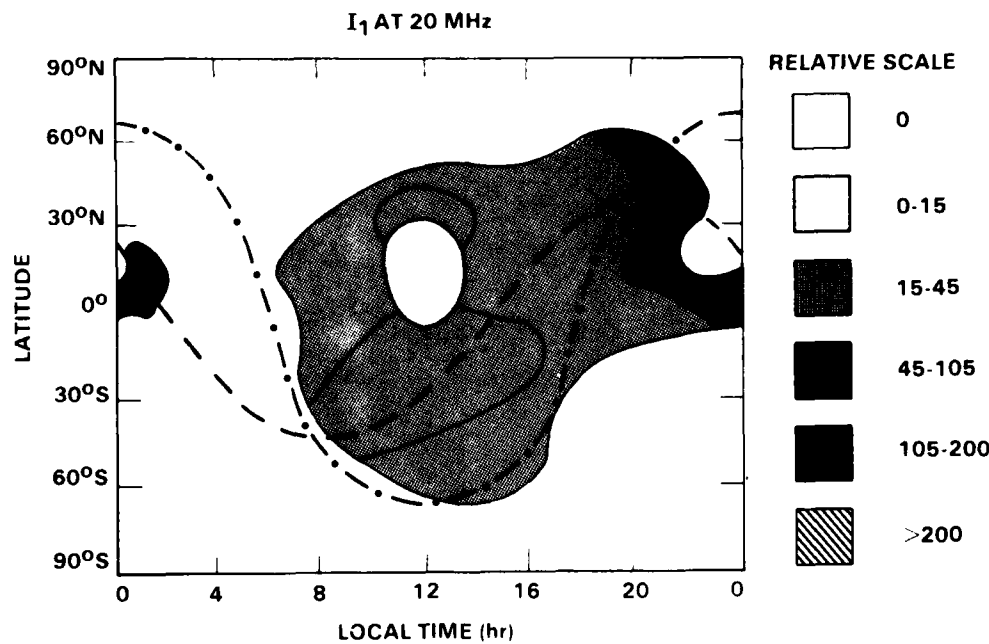


Figure 20. Synoptic Map of Adiabatic Invariant  $I_1$  at  $f=20$  MHz for the IONCAP Model Ionosphere With Sunspot Number 50 in June at 12 UT

#### 7.4 Synoptic $I_{FE}$ Maps

The maps of  $I_{FE}$  (Figure 21 for 8 MHz and Figure 22 for 20 MHz) show the robustness of trapped mode propagation between the E- and F-layers. By comparing Figure 21 with Figure 15 for  $f_oE$ , we see that at 8 MHz this mode is primarily controlled by the E-layer; while comparing Figure 22 with Figures 14 and 15, indicates that at 20 MHz both the E- and the F-layers are influential. Figure 22 also illustrates how the RTW path discussed in Sections 5 and 6 was chosen to pass through regions that were more robust in trapped mode solutions at 20 MHz. A North-South path through the  $60^\circ$  E meridian would probably have been as good or better, but was not used because it would pass through auroral zones, which were not realistically modelled in IONCAP.

#### 8. CONCLUSION

We have shown how the *adiabatic invariant technique* was developed and applied to the problem of describing the propagation modes along great-circle paths (or path segments) in order to qualitatively assess either ground-to-ground, ground-to-satellite or satellite-to-satellite communications. We have demonstrated how to obtain quantitative results in the form of simulated ionograms. We have also indicated how it is possible to obtain a better understanding of global propagation characteristics via synoptic maps of  $I_E$ ,  $I_F$ ,  $I_{FE}$  and  $I_1$ . We have discussed neither how to incorporate absorption effects into ionogram simulation nor how to prepare synoptic maps of absorption. This will be undertaken in future work.

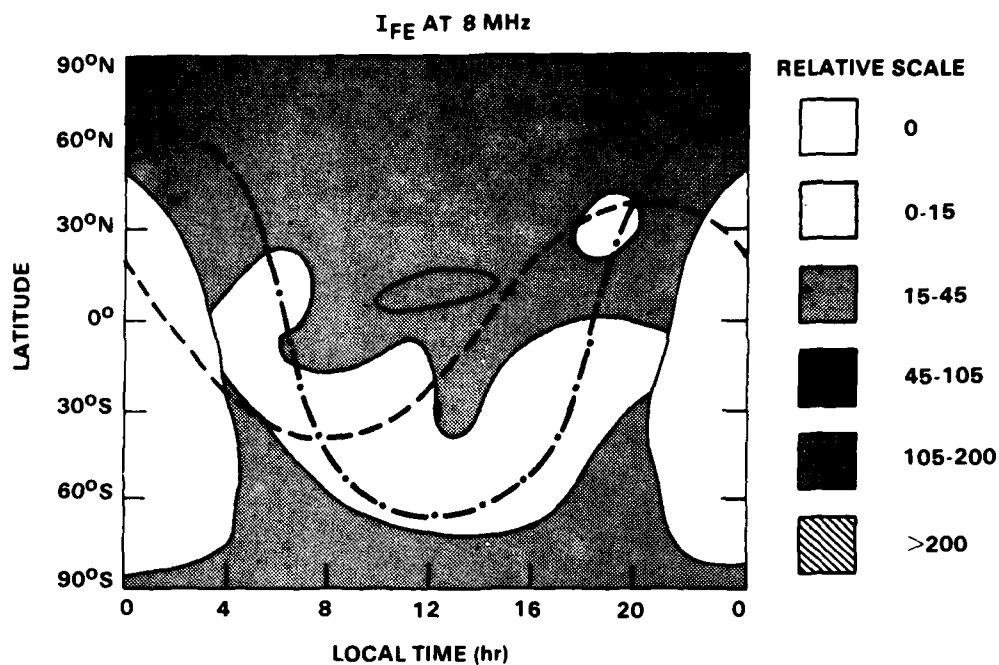


Figure 21. Synoptic Map of Adiabatic Invariant  $I_{FE}$  at  $f = 8$  MHz for the IONCAP Model Ionosphere With Sunspot Number 50 in June at 12 UT

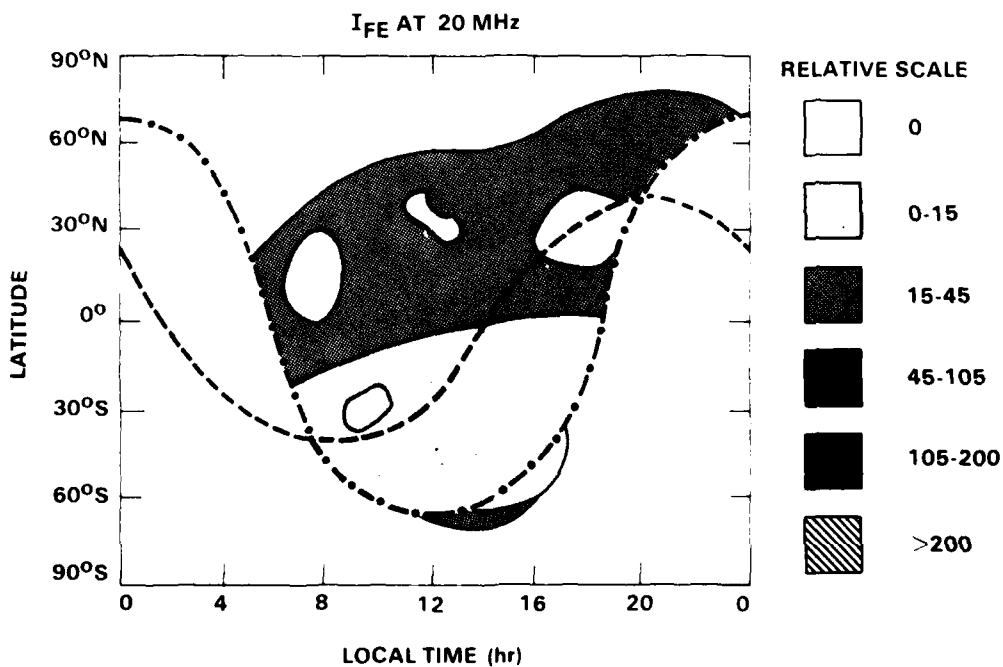


Figure 22. Synoptic Map of Adiabatic Invariant  $I_{FE}$  at  $f = 20$  MHz for the IONCAP Model Ionosphere With Sunspot Number 50 in June at 12 UT

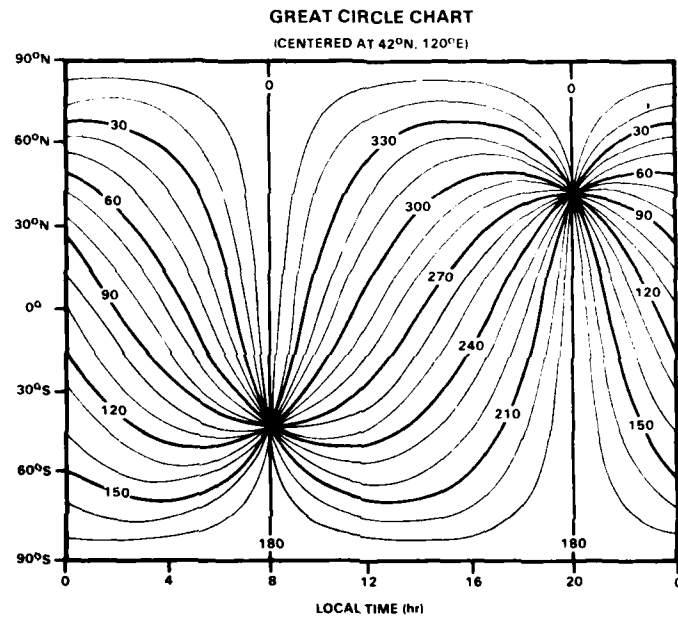


Figure 23. Great Circle Paths Emanating in Various Azimuthal Directions from the Point (42° N, 120° E)

## References

1. Bubenik, D.M., Fraser-Smith, A.C., Sweeney, L.E., Jr., and Villard, O.G., Jr. (1971) Observations of fine structure in high-frequency radio signals propagated around the world, J. Geophys. Res. 76(4):1088-1092.
2. Elkins, T.J., Toman, K., and Sales, G.S. (1980) Theoretical and Experimental Studies of HF Ducted Propagation, RADC-TR-80-360, AD A098944.
3. Tsedilina, Ye. Ye. (1980) Discrete structure of round-the-world signals, Geomagnetism and Aeronomy, 20(1):99-101.
4. Gurevich, A.V. (1971) Effect of nonlinearity on the generation of circumterrestrial signals, Geomagnetism and Aeronomy, 21(6):810-816.
5. Tsedilina, Ye. Ye. (1975) Round-the-world radio wave propagation in ionospheric wave ducts, Geomagnetism and Aeronomy, 15(3):371-374.
6. Fishchuk, D.I., and Tsedilina, Ye. Ye. (1980) Propagation of short radio waves on a mid-latitude round-the-world hop path, Geomagnetism and Aeronomy, 20(3):313-317.
7. Wovk, E., (E. Chvojko) (1959) The refraction of radio waves by a spherical ionized layer, J. Atmos. and Terr. Phys. 16(1/2):124-135.
8. Grinberg, G.A. (1943) Izv. Akad. Nauk SSR, Ser. Fiz. 7:99.
9. Llovd, J.L., Haydon, G.W., Lucas, D.L., and Teters, L.R. Estimating the Performance of Telecommunication Systems Using the Ionospheric Transmission Channel, Vol. 1, Techniques for Analyzing Ionospheric Effects Upon HF Systems, (to be published by NTIA/ITS).
10. Lobachevskiy, L.A., Soares, J., Tushentsova, I.A. Fishchuk, D.I., and Tsedilina, Ye. Ye. (1979) Analysis of the conditions of propagation of decametric radio waves on a long path by the adiabatic method on a fixed frequency. I, Geomagnetism and Aeronomy, 19(3):314-319.
11. Borisov, N.D., Fishchuk, D.I., and Tsedilina, Ye. Ye. (1978) Frequency dependence of the group lag time of round-the-world signals, Radiophysics and Quantum Electronics, 21(3):255-260.

## References

12. Tushentsova, I. A., Fishchuk, D. I., and Tsedilina, Ye. Ye. (1974) Maps of the global distribution of some parameters of ionospheric wave ducts, Preprint No. 5, IZMIRAN.
13. Zacharisen, D. H. World maps of F2 critical frequencies and maximum usable frequency factors, NBS Tech. Note 2 (Apr 1959) and NBS Tech. Note 2/2 (Oct 1960).



*MISSION  
of  
Rome Air Development Center*

*RADC plans and executes research, development, test and selected acquisition programs in support of Command, Control Communications and Intelligence (C<sup>3</sup>I) activities. Technical and engineering support within areas of technical competence is provided to ESD Program Offices (POs) and other ESD elements. The principal technical mission areas are communications, electromagnetic guidance and control, surveillance of ground and aerospace objects, intelligence data collection and handling, information system technology, ionospheric propagation, solid state sciences, microwave physics and electronic reliability, maintainability and compatibility.*

Printed by  
United States Air Force  
Hanscom AFB, Mass. 01731